Continued exposure to Ca results in a shift of the t_{1u} band to greater binding energy and to the development of a tail that intersects the Fermi level (see Fig. 2, spectrum f). This tail gives the initial indication of the filling of the t_{1g} band. Doubling the exposure (spectrum g) results in a shift of the entire spectrum to larger binding energy and in the appearance of a new peak associated with the t_{1g} band. At this exposure the rounded cutoff indicates an inhomogeneous surface, that is, that excess Ca is left on surface after annealing. The separation of the peaks of the two bands in spectrum g is ~1 eV, in accord with the separation in the empty bands in the calculation of Saito and Oshiyama (6). If the Ca atoms are fully ionized, four atoms in the octahedral site, together with one in each of the two tetrahedral sites per C_{60}, can provide 12 electrons to fill both the t_{1u} and t_{1g} bands without a structural phase transition. In spectrum g the t_{1g} band clearly intersects the Fermi level, indicating that the composition has not quite reached that of Ca_6C_{60} or is not quite ionic. The data show that the system is metallic both as the t_{1u} band is filling and subsequently as the t_{1g} band is occupied.

Because the escape depth in C_{60} is smaller than the molecular diameter, we must consider the possibility that the two peaks in Fig. 2, spectrum g, are due, not to the t_{1u} and t_{1g} bands as proposed above, but to a splitting of the surface t_{1u} band. We have invoked this splitting to account for the weakness of the Fermi cutoff in Fig. 2, spectra b to d. The fact that the two peaks in spectrum g have comparable intensities is incompatible with the split-band picture, which requires to a 2:1 intensity ratio. It is in accord with the two-band picture, because both bands are threefold degenerate (6). Moreover, the total area of the two components is too large as compared to that of the h_u band to be due the split t_{1u} band alone. We therefore rule out the split surface-band interpretation.

Data taken with the C_{60}-Ca sandwich are shown in Fig. 3. The sample was allowed to warm up from liquid N_2 temperature to room temperature, was held there for some time, and was then annealed for 1 min at progressively higher temperatures. The data taken at low temperature fail to show a Fermi edge. This is no surprise because an anneal was required to produce a Fermi edge after room-temperature exposure to Ca. A spectrum indicative of a filled t_{1u} band is reached just below room temperature in Fig. 3, spectrum f, where the work function indicates that Ca has reached the surface. By 375 K, the t_{1g} state appears to be fully occupied, corresponding to the compound Ca_6C_{60}. The metallic character is not apparent in these spectra, suggesting that there is rapid conversion to the fully doped compound Ca_6C_{60} when Ca is plentiful. The work function cutoff continues to move to larger energy, indicating that Ca is accumulating on the surface.

Finally we must consider the possibility that the filled t_{1g} band is a surface phenomenon associated with the presence of excess Ca on the surface. The data in Fig. 2 do not suffice to rule this out, because the filled t_{1g} band is seen only in spectrum g where the broadened work function cutoff indicates an inhomogeneous surface. However, the data in Fig. 3, spectra h through k, show the t_{1g} band filled well before excess Ca has accumulated on the surface, indicating that it is not a surface phenomenon. We conclude that the photoemission spectra show the progressive occupancy of the bulk t_{1u} and t_{1g} bands, with evidence of metallic conductivity for the incompletely filled bands. It is then clear that the superconductivity of Ca_5C_{60} is due to the t_{1g} band, which can be filled without a structural change because of the small size of the Ca ion.

REFERENCES AND NOTES

1. A. R. Kortan *et al.*, *Nature* **355**, 529 (1992), and references therein.
2. Y. Chen, F. Stepniak, J. H. Weaver, L. P. F. Chibante, R. E. Smalley, in preparation.
3. C. Gu *et al.*, *Phys. Rev. B* **45**, 6348 (1992).
4. G. K. Wertheim and D. N. E. Buchanan, in preparation.
5. ———, E. E. Chaban, J. E. Rowe, *Solid State Commun.* **83**, 785 (1992).
6. S. Saito and A. Oshiyama, *Phys. Rev Lett.* **66**, 2637 (1991).

7. We are indebted to R. C. Haddon for the purified C_{60} used in these experiments and to E. E. Chaban for the construction of the Ca and C_{60} furnaces.

30 July 1992; accepted 24 September 1992

Electronic, Magnetic, and Geometric Structure of Metallo-Carbohedrenes

B. V. Reddy, S. N. Khanna, P. Jena

The energetics and the electronic, magnetic, and geometric structure of the metallo-carbohedrene Ti_8C_{12} have been calculated self-consistently in the density functional formulation. The structure of Ti_8C_{12} is a distorted dodecahedron with a binding energy of 6.1 electron volts per atom. The unusual stability is derived from covalent-like bonding between carbon atoms and between titanium and carbon atoms with no appreciable interaction between titanium atoms. The density of states at the Fermi energy is high and is derived from a strong hybridization between titanium 3*d* and carbon *sp* electrons. Titanium sites carry a small magnetic moment of 0.35 Bohr magneton per atom and the cluster is only weakly magnetic.

Recently Guo, Kerns, and Castleman (*1*) reported the observation of an unusually stable cage-like network consisting of eight Ti and twelve C atoms (Ti_8C_{12}). This cluster, known as metallo-carbohedrene or "met-car," shares a common shape with buckminsterfullerenes (*2*). However, there are fundamental differences between these two clusters. In the fullerenes all the atoms are C atoms and they are arranged in pentagonal and hexagonal rings, whereas in met-cars there are only pentagons whose vertices are occupied by metal and C atoms. It is likely that the presence of metal atoms may give the met-cars unusual electronic and magnetic properties. Possible applications of met-cars for new electronic materials, pollution control, and chemical tracers, and in site-specific protein chemistry in living organisms are being envisioned.

Guo *et al.* (*1*) assigned a dodecahedral structure to the met-cars that is characterized by twelve pentagons with Ti occupying eight identically coordinated sites. Each Ti is bonded to three C atoms, and each C is bonded to two Ti and one C atom. Guo *et al.* arrived at this structure by studying its reaction with NH_3 and by following the general rules of chemical bonding.

Aside from the proposed structure of met-car and its apparent stability, little is known about its electronic structure, the reasons for its unusual stability, its geometrical parameters, and its electronic and magnetic properties. To provide some understanding of these quantities, we undertook a series of fully self-consistent total energy calculations of Ti_8C_{12}. Our method is based on the self-consistent field–linear combination of atomic orbitals–molecular orbital (SCF-LCAO-MO) theory and the density functional approximation (*3*). Our results show that the unusual stability of Ti_8C_{12} is derived from a large binding energy (~6.1 eV per atom) owing to covalent bonding between C atoms and between Ti and C atoms. There is virtually no interaction between Ti atoms. The electron density of states at the Fermi energy is high

Physics Department, Virginia Commonwealth University, Richmond, VA 23284.

and is composed of Ti *d* electrons hybridized with C *sp* electrons. The geometrical structure is not a perfect dodecahedron but a distorted one with the C–C bond being the shortest distance and the Ti–Ti bond the longest distance. There is only a small "puckering" of the cage-like structure where the C atoms lie on a sphere whose radius is 0.1 atomic unit [(au), where the unit of length is the Bohr radius] smaller than that containing the Ti atoms. The met-car is only weakly magnetic.

To describe our theoretical procedure, we begin by writing the eigenfunctions of the cluster as molecular orbitals, Ψ_i, composed of an LCAO, $\phi(r - R_j)$, centered on the atomic site R_j, namely:

$$\Psi_i(r) = \sum_j C_{ij}\phi_j(r - R_j) \quad (1)$$

where the C_{ij}'s are the variational coefficients determined from the solution of the Rayleigh-Ritz equation,

$$(H - ES)\,C = 0 \quad (2)$$

where C is the matrix, E is energy, S is the overlap integral, and H is the Hamiltonian. The one-electron Hamiltonian is expressed in density functional theory as (*3*)

$$H = -\frac{1}{2}\nabla^2 + \int \frac{n(r')d^3r'}{|r - r'|} + \sum_j \frac{Z_j}{|r - R_j|} + V_{XC} \quad (3)$$

Here $n(r')$ is the electron density of spin-up and spin-down electrons and Z_j is the charge on the jth nucleus; V_{XC} is the exchange-correlation potential for electrons, and we calculate it using the local density approximation to the density functional theory. Equations 1 through 3 are then solved self-consistently.

We followed two different but complimentary schemes to solve Eqs. 1 through 3. The first one is based on the discrete variational method (DVM) where the atomic orbitals ϕ_j are numerical functions obtained by solving the atomic Schrödinger equation (*4*). The secular equation (Eq. 2) is then solved by calculating the matrix elements on a three-dimensional grid of random points (*4*). This is computationally an efficient method, although the choice of the numerical atomic orbitals does restrict the variational freedom and an accurate determination of the energy integrals does require the use of a large number of grid points. To ensure consistency in our results, we also used another approach (*5*), the linear combination of Gaussian-type orbitals (LCGTO), where the atomic functions, fitted to a complete set of Gaussian basis functions, offer larger variational freedom.

In the DVM approach (*4*), the (atomic) configuration for Ti and C consisted of (3*d*, 4*s*, and 4*p*) and (2*s*, 2*p*) orbitals, respectively. The inner cores were frozen. In the LCGTO approach (*5*), the basis sets consisted of (5*s*, 1*p*, and 3*d*) uncontracted Gaussian functions for Ti and (5*s*, 4*p*) uncontracted Gaussian functions for C. The inner cores were replaced by norm-conserving pseudopotentials (*6*). The details of these methods have been described (*5*).

To obtain the geometry of Ti_8C_{12}, we started with the ideal dodecahedral structure suggested by Guo *et al.* (*1*). Because this structure consisting of two different atoms has high symmetry (T_h) and can undergo Jahn-Teller distortion, we have used the C_{2V} symmetry and allowed the Ti–Ti, Ti–C, and C–C distances to vary independently to minimize the energy. The resulting equilibrium geometry of Ti_8C_{12} is given in Fig. 1. The corresponding Ti–Ti, Ti–C, and C–C distances calculated by the use of LCGTO and DVM methods are given in Table 1.

If we compare the results between the two theoretical methods, we find that the bond distances between C–C, Ti–C, and Ti–Ti calculated by the two approaches are comparable to each other, as are the binding energy per atom and the vertical ionization potential, which is the energy necessary to ionize the neutral cluster without changing its geometry. The small discrepancy between these two sets of results stems not only from the different numerical procedures used, but more importantly from the treatment of the exchange-correlation potential. In the DVM we used the spin-density functional form because of the interest in magnetism, whereas in the LCGTO we ignored the spin. This was necessary because our LCGTO code makes no use of cluster symmetry and consequently is computer-intensive. Including spin would make the LCGTO a prohibitive task. However, the near agreement between these two sets of results reaffirms our belief that the physics of the problem discussed in the following is independent of the method we use.

We now discuss the geometry of Ti_8C_{12}. We note from Table 1 that the C–C bond is shorter than the Ti–C bond by about 20%, whereas the Ti–Ti distance is larger by about a factor of 2 than the C–C distance. This result illustrates that the dodecahedron undergoes distortion, and the pentagonal ring consisting of two Ti and three C atoms is an irregular one. The pentagon containing two Ti and three C atoms, however, deviates little from the planar structure because all the C atoms lie on a sphere of radius of 4.9 au whereas all Ti atoms lie on a sphere of radius of 5.0 au. Thus the "puckering" of the cage-like structure of the met-car is only minimal.

The C–C bond in Ti_8C_{12} is 2.86 au, which is only slightly elongated from the C_2 dimer bond length of 2.35 au obtained by us. Thus, the C–C bond in Ti_8C_{12} deviates little from the conventional covalent bond.

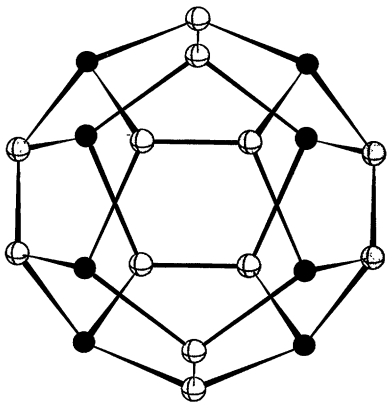

Fig. 1. Geometrical structure of Ti_8C_{12}. The filled circles are Ti sites and the shaded circles represent C sites.

Table 1. Bond lengths, binding energy, ionization potential, magnetic moments at the Ti site, and the Mulliken population analysis for the Ti_8C_{12} cluster.

Parameter	DVM	LCGTO
Bond length (au)		
C–C	2.86	2.78
Ti–C	3.71	3.79
Ti–Ti	5.77	5.06
Binding energy per atom (eV)	6.1	6.62
Ionization potential (eV)	5.97	6.02
Moment at the Ti site (μ_B)	0.35	
Mulliken population (e^-)		
Ti	+1.07	+0.66
C	−0.71	−0.44

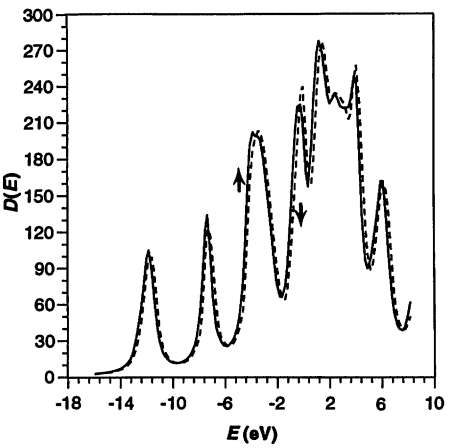

Fig. 2. Electronic spin density of states, $D(E)$, as a function of energy in Ti_8C_{12}. The Fermi energy is located at $E = 0$. The solid and the dashed lines correspond to spin-up and spin-down electrons, respectively.

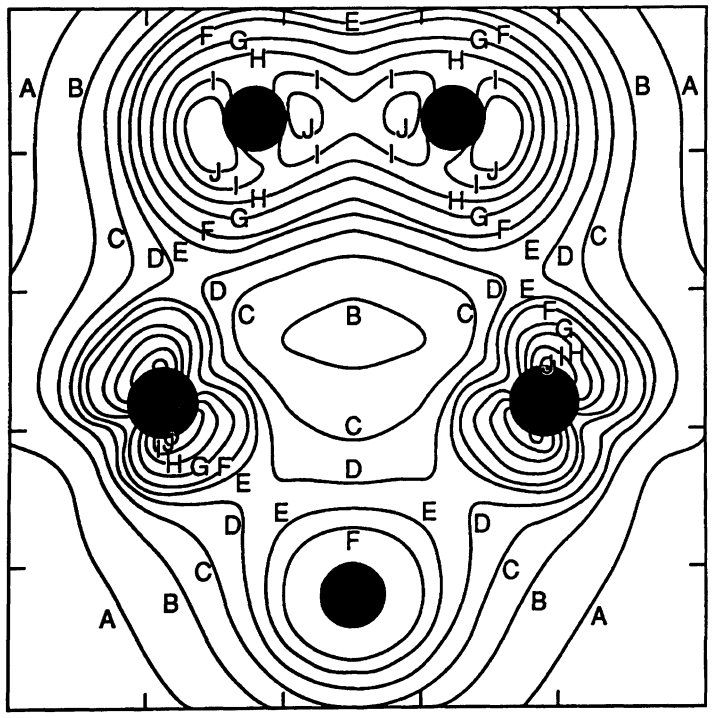

Fig. 3. Charge density profile (in atomic units) of a pentagonal face of Ti_8C_{12}. The upper two atoms and the bottom atom are C sites, and the middle two atoms are Ti sites. The bottom C is slightly off the plane.

The nature of bonding between Ti and C in met-cars, however, is quite different from that in stoichiometric TiC (*7*). In TiC the Ti–C distance is 4.09 au, which is larger than the corresponding distance of 3.71 au in Ti_8C_{12}. This difference results from much stronger bonding between Ti–C in Ti_8C_{12} than in TiC.

The strong C–C and Ti–C bonds are what gives Ti_8C_{12} its unusual stability. The total binding energy of Ti_8C_{12} is 132.4 eV or 6.62 eV/atom in the LCGTO approach. This is quite large indeed and comparable to the cohesive energy of stoichiometric TiC (7.1 eV). The large binding energy of the met-car is derived primarily from the C–C and the Ti–C bonding. This can be easily seen if we count the bond energies in Ti_8C_{12}. There are 24 Ti–C bonds and 6 C–C bonds in Fig. 1. Our calculated binding energies (bond length) of Ti–C and C–C are, respectively, 4.6 eV (3.0 au) and 6.6 eV (2.35 au). This would lead to a bond energy of 150 eV for Ti_8C_{12}. The calculated binding energy is higher than the actual binding energy of Ti_8C_{12} because Ti carries a large positive charge in the met-car, as can be seen from the Mulliken analysis in Table 1. Consequently, the Ti atoms repel each other, which results in an increase in the Ti–C and C–C distances as compared to the corresponding values in the dimers. The large vertical ionization potential (6 eV) of Ti_8C_{12} also adds to its stability.

To examine the electronic structure of Ti_8C_{12}, we have calculated the total electron density of states (DOS), charge density profile, and Mulliken charge. In an MO calculation the electron energy levels are discrete. To simulate the conventional density of states, it is customary to broaden the energy levels by using a smearing function. We used a Lorentzian of width 0.4 eV to broaden the one-electron levels. The resulting density of states is plotted in Fig. 2. The DOS is marked by peaks at −11.8, −7.3, and −3.67 eV that can be identified as associated with C sites. In addition, there is a broadened band extending from −1.4 to 7 eV that arises because of the strong hybridization of Ti 3*d* and C *sp* electrons. The Fermi energy lies in this hybridized manifold, and the DOS at the Fermi energy is high, carrying the signature of metallicity.

To determine whether the metallic character arises from completely delocalized electrons, we have calculated the electron density profiles in a Ti_2C_3 pentagonal ring. The results are plotted in Fig. 3. There is a significant pile-up of electrons along the C–C and Ti–C bonds; there is very little electron concentration at the center of the pentagonal ring or along the Ti–Ti "bond." This picture is consistent with the short C–C and Ti–C bonds as discussed earlier and with the Mulliken charge analysis, which indicates significant charge transfer from Ti to C. Titanium is known to be more electropositive than C.

We next discuss the possibility that Ti_8C_{12} could be magnetic. Although all the transition metal atoms are magnetic as a result of Hund's rule coupling, only Fe, Co, and Ni are magnetic in the bulk phase. However, otherwise nonmagnetic transition-metal atoms such as V and Ti could become magnetic if their coordination numbers could be reduced by being confined to one or two dimensions or to small clusters (*8*). The magnetism results as the overlap between electron orbitals is reduced. In Ti_8C_{12}, the interactions between two Ti atoms are minimal. This should cause Ti to carry a large moment. However, the proximity of Ti to a nonmagnetic atom such as C would tend to reduce this moment (*9*).

To see how these factors compete, we have calculated the spin-density distribution in Ti_8C_{12} by carrying out a spin-polarized calculation using the DVM method. The spin-dependent densities of states are plotted in Fig. 2. One can calculate the magnetic moment at any site by integrating the partial spin density of states up to the Fermi energy. The result is given in Table 1. The moment on the Ti atom is quite small [0.35 Bohr magneton (μ_B)], and the moment on C is negligible. The atomic configuration of Ti is $3d^3\ 4s^1$ and can support a moment of 4.0 μ_B. Thus, the substantial reduction in the moment of Ti is a direct consequence of its bonding with C.

It is worth wondering if other met-cars involving C and transition-metal systems such as Sc, V, Cr, Mn, Fe, Co, or Ni would exhibit properties similar to those of Ti_8C_{12}. We have begun a systematic study of this problem and present here the results on V_8C_{12}. We found that this cluster also is very stable with a binding energy per atom of 5.7 eV and a vertical ionization potential of 4.3 eV. The geometry is similar to that of Ti_8C_{12} with C–C, V–C, and V–V distances of 2.86, 3.5, and 5.27 au, respectively. The bonding between C–C and V–C is also of covalent character, and the moment on V is small, namely, 0.32 μ_B. Whether these properties will be common to met-cars containing Fe, Co, and Ni remains to be seen.

It is appropriate to ask whether the met-cars are another class of fullerenes. Comparison of the present results with the available calculations on C_{60} indicates that the bond lengths and binding energies are similar. For example, the C–C bond lengths of 2.65 and 2.76 au in C_{60} (*10*) are comparable to the corresponding bond length of 2.78 au found here. The binding energy per atom of 6.1 eV and vertical ionization potential of 6.0 eV in Ti_8C_{12} are comparable to the corresponding values of 7.4 eV (*11*) and 7.6 ± 0.2 eV (*12*) in C_{60}. All these comparisons suggest that the met-cars, like C_{60}, are another class of very

stable clusters. However, in contrast to C_{60}, the metallic Ti atoms in Ti_8C_{12} not only stabilize the structure composed entirely of pentagons but also give it a unique electronic structure that is characterized by the Fermi energy lying in the middle of the band. One therefore does not have to dope a met-car to make it conducting as is necessary for C_{60} (*13*).

REFERENCES AND NOTES

1. B. C. Guo, K. P. Kerns, A. W. Castleman, Jr., *Science* **255**, 1411 (1992); *J. Phys. Chem.*, in press.
2. R. F. Curl and R. E. Smalley, *Sci. Am.* **265**, 54 (October 1991); H. W. Kroto, J. R. Heath, S. C. O'Brien, R. E. Curl, R. E. Smalley, *Nature* **318**, 162 (1985).
3. P. Hohenberg and W. Kohn, *Phys. Rev.* **136**, B864 (1964); W. Kohn and L. J. Sham, *ibid.* **140**, A1133 (1965).
4. D. E. Ellis, *Int. J. Quantum Chem.* **S2**, 35 (1968); M. R. Press, S. N. Khanna, P. Jena, *Phys. Rev. B* **36**, 5446 (1987).
5. J. L. Martins, J. Buttet, R. Car, *Phys. Rev. B* **31**, 1804 (1985); F. Reuse, S. N. Khanna, V. de Coulon, J. Buttet, *ibid.* **41**, 11743 (1990).
6. G. B. Bachelet, D. R. Hamann, M. Schluter, *ibid.* **26**, 4199 (1982).
7. W. B. Pearson, Ed., *A Handbook of Lattice Spacings and Structures of Metals and Alloys* (Pergamon, New York, 1967).
8. F. Liu, S. N. Khanna, P. Jena, *Phys. Rev. B* **43**, 8179 (1991).
9. M. R. Press, S. N. Khanna, P. Jena, M. J. Puska, *Z. Phys. B* **81**, 281 (1990).
10. C. S. Yannoni, P. Bernier, D. S. Bethune, G. Meijer, J. R. Salem, *J. Am. Chem. Soc.* **113**, 3190 (1991).
11. S. Saito and A. Oshiyama, *Phys. Rev. Lett.* **66**, 2637 (1991).
12. J. H. Weaver *et al.*, *ibid.*, p. 1741.
13. M. J. Rosseinsky *et al.*, *ibid.*, p. 2830.

14. This work was funded in part by a grant from the Department of Energy (DE-FG05-87ER45316). One of the authors (B.V.R.) is supported by the Army Research Office (DAAL-03-89-K-0015) for work in magnetism. We thank A. W. Castleman, Jr., for sharing his results. One of us (S.N.K.) is grateful to F. Reuse and J. L. Martins for help in local density calculations. We are grateful to B. B. Brown and other members of Academic Computing for the computational facilities.

20 July 1992; accepted 21 September 1992

Temperature and Size Variabilities of the Western Pacific Warm Pool

Xiao-Hai Yan,* Chung-Ru Ho, Quanan Zheng, Vic Klemas

Variabilities in sea-surface temperature and size of the Western Pacific Warm Pool were tracked with 10 years of satellite multichannel sea-surface temperature observations from 1982 to 1991. The results show that both annual mean sea-surface temperature and the size of the warm pool increased from 1983 to 1987 and fluctuated after 1987. Possible causes of these variations include solar irradiance variabilities, El Niño–Southern Oscillation events, volcanic activities, and global warming.

The Western Pacific Warm Pool (WPWP) covers more of the earth's surface than does the continental United States. It stands out vividly as the orange and red area in our newly processed image of long-term average sea-surface temperature (SST) obtained from satellite data (Fig. 1). This swath of ocean near New Guinea has a temperature consistently higher than 28°C (*1*), about 2° to 5°C higher than that of other equatorial waters, and is the largest single expanse of warm water on our planet.

In recent years, significant international efforts have been made to understand the coupled atmosphere system in the equatorial ocean. However, most oceanographic studies have focused on the eastern and central Pacific Ocean with less effort given to the WPWP, although the early stages of the El Niño–Southern Oscillation (ENSO) phenomenon may first develop there (*2*). Therefore, it is important to track the warm pool as its temperature and size fluctuate from year to year and to understand the relation of these dynamics and ENSO events to global climate changes. To track the changes in the WPWP, we analyzed multichannel SST (MCSST) data from the Television and Infrared Observation Satellite–National Oceanic and Atmospheric Administration (TIROS-N–NOAA) series Advanced Very High Resolution Radiometer (AVHRR). This MCSST product consists of a weekly composite of the globe and regional subsets at a resolution of ~18 km. We used the weekly MCSST for the tropical Pacific Ocean from 1982 to 1991 to compute monthly mean SST, annual mean SST, and long-term mean SST.

The TIROS-N–NOAA series polar orbiting satellites carry four-channel (TIROS-N, NOAA-6, NOAA-8, and NOAA-10) or five-channel (NOAA-7 and NOAA-9) AVHRR sensors. Each sensor has an instantaneous field of view that corresponds to a ground resolution of about 1.1 km at nadir as well as a total scan field of view of ±55.4° from nadir (approximately 2240 km). The five spectral bands measured are as follows: channel 1, visible, 0.58 to 0.68 μm; channel 2, near infrared, 0.725 to 1.10 μm; channel 3, infrared, 3.55 to 3.99 μm; channel 4, thermal infrared, 10.2 to 11.5 μm; and channel 5, thermal infrared, 11.5 to 12.5 μm (NOAA-7 and NOAA-9).

MCSST values are binned into 2048 by 1025 pixel grids. Then, for each grid point the average of all MCSST measurements available for 1 week is computed. Open areas are interpolated with an iterative Laplacian relaxation technique until all such areas connected to valid observations are filled. A first estimate for open areas is provided by computation of the mean of horizontal, bounding data-filled pixels. The original global weekly MCSST data are 16 bits, and the temperatures are these values divided by 10. Thus, the resolution of MCSST is 0.1°C with an overall calibration error of ±0.2°C (*3*). The weekly MCSST is first averaged into monthly mean MCSST. The annual mean MCSST and long-term mean MCSST are then averaged again from monthly mean and annual mean MCSST, respectively.

Figure 1 shows the vast WPWP, which has the highest open-ocean water temperatures in the world. The pattern of the long-term mean SST from calibrated satellite AVHRR data is close to that of the obser-

Fig. 1. Color-enhanced image of 10-year mean (1982 to 1991) SST from satellite data, with warmest surface temperature evident in the WPWP (orange and red).

Center for Remote Sensing, Graduate College of Marine Studies, University of Delaware, Newark, DE 19716.

*To whom correspondence should be addressed.